Experiments-Guided Modeling of MCM-41: Impact of Pore Symmetry on Gas Adsorption

*Paola Carta, Claudio Cara, Carla Cannas, and Mariano Andrea Scorciapino**

P. Carta, C. Cara, C. Cannas, M. A. Scorciapino
Department of Chemical and Geological Sciences - University of Cagliari - Cittadella Universitaria di Monserrato - SP 8 km 0,700 - Monserrato (CA), 09042, Italy.
E-mail: scorciapino@unica.it

C. Cara
Present Address: Fluorsid S.p.a. - Area Industriale di Cagliari - II Strada Macchiareddu - Assemini (CA), 09032, Italy.

Keywords: Molecular Dynamics, Grand Canonical Monte Carlo, mesostructured silica, porous materials, adsorption isotherms, P6mm / P4mm space group symmetry

Among mesoporous ordered silica-based materials, MCM-41 is widely employed in both experimental and computational investigations of gas adsorption. Specific surface area and pore size distribution are typically obtained by analyzing the N_2 adsorption isotherm. To this aim, different models and theories are available, and which one is more accurate is under debate. On the computational side, the in-silico model ought to match the characteristics of real samples and to reproduce the macroscopic performance. While the typical hexagonal symmetry is usually considered, the tetragonal one is sometimes applied without any explained rationale. Interestingly, during the last decade, the preparation of mesoporous silica-based materials with rare tetragonal symmetry was reported, indeed, but these being never tested as gas sorbents. In the present work, computer models with different symmetry are compared for their ability to reproduce the available experimental data from real samples. The combination of grand-canonical Monte Carlo and molecular dynamics simulations is used to probe the differences at the microscopic level. The surface-adsorbed gas molecules are differently ordered and a different type of N_2 adsorption isotherm is correspondingly found.

1. Introduction

Mesoporous silica-based materials have received, and continue to receive, much attention because of their widespread use in many fields, such as, selective adsorption and separation, capture and storage, and catalysis. The extremely high surface area, together with the highly uniform pore size, make them so attractive. In addition, the existence of many approaches to tailor their surface chemico-physical properties and, thus, to obtain technologically advanced materials, justifies the interest of the scientific community and the ever-increasing number of new applications.[1–10]

In 1992, a family of silicate (M41S) and aluminosilicate mesoporous materials (pore diameter between 2 and 50 nm) was obtained at Mobil Corporation Laboratories,[2,11] by combining sol-gel synthesis with a proper surfactant templating agent. The latter was not a single solvated organic or inorganic species, but a self-assembled surfactant array. Three main mesophases are typically produced, namely, the cubic MCM-48, the lamellar MCM-50 and the hexagonal MCM-41. The latter is characterized by a regular 2D hexagonal array (*P6mm* space group symmetry) of highly uniform parallel non-interconnected channels, with the pore diameter depending on the specific templating agent. Compared to the other members of the M41S mesoporous family, MCM-41 has a higher thermal stability, and it is easier to prepare, thus attracting greater attention.[1,12]

The ordered pore architecture of MCM-41 can be clearly observed through transmission electron microscopy (TEM)[2,13] and assessed through low-angle x-ray diffraction (LA-XRD) techniques or small-angle x-ray scattering (SAXS).[2] Overall, porosity can be as high as 80%, with the pore walls composed by amorphous silica.[1] The analysis of the N_2 adsorption isotherms according to the Brunauer–Emmett–Teller (BET) theory[14] is widely employed to estimate the Specific Surface Area (SSA), which is typically larger than 700 m^2/g.[11] Analysis of the same adsorption isotherm through the Barrett-Joyner-Halenda (BJH) model[15] is the typical choice to determine the pore size distribution (PSD). However, other approaches are available to retrieve these textural details, which are more recent and have a more rigorous physical base, such as the Density Functional Theory (DFT), allowing the determination of both the SSA, the pore volume and the PSD.[16] The former models and theories have been recently questioned.[17]

Computer calculations and simulations are able to unveil the microscopic details and the energetic aspects of the interaction between the guest molecules and the solid surface. Adsorption capacity, selectivity, diffusivity, and so on, can be investigated at the microscopic level under different pressure, temperature and humidity, so to obtain fundamental information

to tailor material synthesis and functionalization to meet specific goals. Computational approaches can be used to complement the experiments, but also to possibly predict the system behavior, and to save time and resources on the laboratory bench. To this aim, the preparation of a 3D model that matches the characteristics of the real sample and that is able to reproduce the macroscopic behavior, as seen by the experiments, is crucial. Mesoporous materials cannot be modeled as simple flat surfaces or slits. At the mesoscale, pore radius, curvature, density and symmetry should be taken into account.

Many computational works are present in the literature on MCM-41 as gas sorbent. Although the typical *P6mm* symmetry of MCM-41 is correctly modelled in many investigations,[18–23] several works were based on almost square simulation boxes and a resulting tetragonal pore symmetry.[24–26] It is not reported, however, why this choice was taken and whether such a marked change of symmetry on the mesostructure had an impact on the results.

In 2009, Jin et al.[27] reported the preparation of silica-based mesostructured materials with a rare tetragonal *P4mm* symmetry for the first time, as far as we are aware. DNA helices, instead of the typical surfactants for MCM-41 synthesis, were used as the templating agent. Later on, the progress in silica biomineralization templating was reported by the same research group, by using several classes of helical biomolecules, including DNA, polypeptides, cellulose and rod-like viruses, and showing the possibility of tuning the pore size, hierarchical structure and morphology of this new class of *P4mm* mesoporous materials by changing the synthesis conditions and the relative concentration of chemicals.[28–32] Recently, the confinement of ultrasmall metal/metal oxide nanoparticles within the mesopores was also achieved.[33] However, these materials have not been tested yet for their performance as gas sorbents and molecular sieves. As far as we are aware, not even a single N_2 adsorption isotherm has been reported so far.

In this work, different computer models of MCM-41 have been generated, based on the outcomes of the experimental characterization of a real sample, through a series of complementary techniques, namely, TEM, LA-XRD, N_2 adsorption isotherm, and solid-state nuclear magnetic resonance (SS-NMR). A different average pore diameter resulted from the experiments, depending on whether the BJH or DFT model was applied to analyze the N_2 adsorption isotherm. Correspondingly, a different value for the pore-wall thickness was obtained. In addition, a different SSA resulted from the experiments, depending on whether the BET or DFT was applied to the N_2 adsorption isotherm. Thus, computational models of MCM-41 with different pore size but the same canonical hexagonal *P6mm* symmetry were compared, in agreement with the experiments performed on the real sample. In addition, models of

mesoporous materials with the same pore size, the same lattice parameter but the rare tetragonal *P4mm* symmetry were investigated. In-silico models were analyzed and compared in terms of the ability to reproduce the experimental N_2 adsorption isotherm. By using a combination of Grand-Canonical Monte Carlo (GCMC) and Molecular Dynamics (MD) simulations, the differences in the performance were rationalized in terms of the microscopic details of the models, unveiling interesting differences of the adsorption process among the *P6mm* and the *P4mm* models. This work also shows the potential risks of using some of the most common characterization techniques on mesostructured silica, whose results simply cannot fit in a reliable tridimensional model.

2. Results and Discussion

The LA-XRD pattern (**Figure 1**a) proves the formation of the MCM-41, as confirmed by the typical reflections [100], [110] and [200], which can be ascribed to the *P6mm* hexagonal pore structure. The narrow signals are clear indication of the high-quality order of the mesoporous structure.

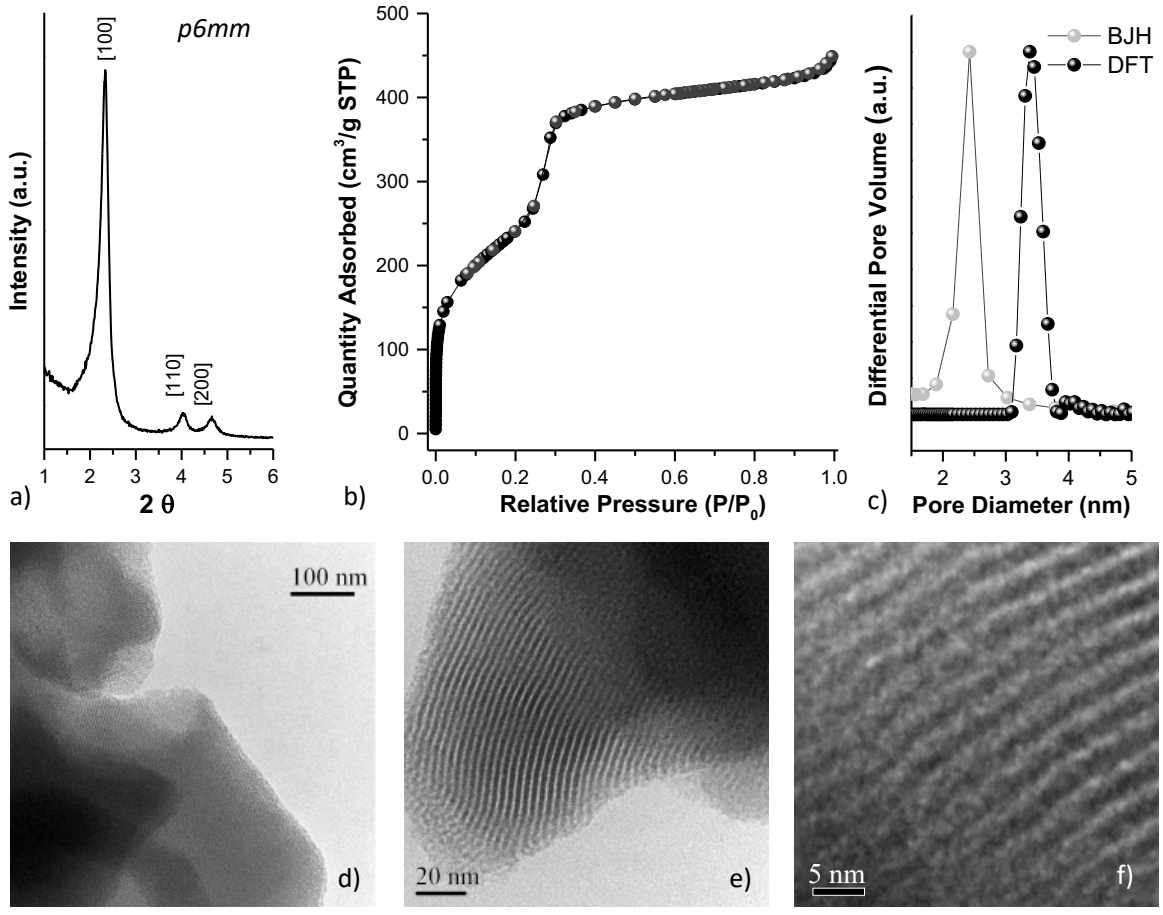

Figure 1. LA-XRD **(a)**, N_2-physisorption isotherms **(b)**, PSD calculated by BJH and DFT models **(c)**, TEM images at different magnification **(d-g)** of the MCM-41 sample.

The N_2-physisorption isotherm (Figure 1b) is classified as IV-B, on the basis of IUPAC classification.[34] This is commonly attributed to mesoporous materials such as MCM-41, which is characterized by the presence of a clear step at about 0.3 p/p_0, due to capillary condensation inside the mesopores. When PSD was calculated with either BJH or DFT (Figure 1c), different average pore size was obtained, 2.4 and 3.4 nm, respectively. As reported in the literature, the average pore size estimated by the DFT model is typically about 1 nm larger than that obtained by BJH.[4,35]

TEM images at different magnification (Figure 1d-g) depict the features of the mesostructured silica, with 2D-pore structure made up of parallel mesochannels, regularly separated by amorphous silica walls. The limit of TEM is that it does not allow to accurately estimate the pore size and the wall thickness, since the optimal alignment of the electron beam with the C_6 axis of symmetry is rarely achieved.[36] These textural properties of the MCM-41 sample are reported in Table 1.

Table 1. Textural properties of MCM-41 silica.

SSA BET [m^2g^{-1}]	SSA DFT [m^2g^{-1}]	Pore Volume [cm^3g^{-1}]	PSD BJH [nm]	PSD DFT [nm]	d_{100} [nm]	a_0 [nm]	wall thickness BJH [nm]	wall thickness DFT [nm]
877	725	0.69	2.4	3.4	3.8	4.4	2.0	1.0

Figure 2 shows the ^{29}Si-MAS SS-NMR spectrum obtained from the MCM-41 sample. Three components were observed, whose chemical shift and relative intensity (Figure 2) are in agreement with the literature.[4,37,38]

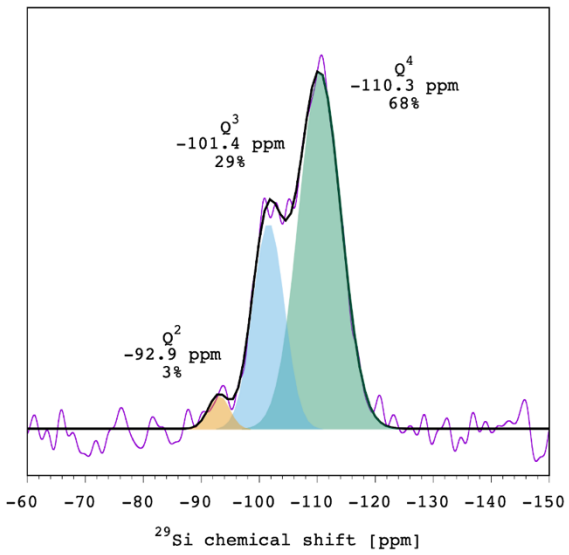

Figure 2. ^{29}Si MAS SS-NMR spectrum (purple) together with deconvolution (black) into three components. Q^4, Q^3 and Q^2 silicon-types are shown as shaded gaussian contributions to the total spectrum, with the corresponding chemical shift and atomic percentage.

The Q^4 component is attributed to the bulk Si atoms, which are involved in 4 siloxane bridges. The Q^3 and Q^2 components are due to surface Si atoms with a single and two geminal silanol groups, respectively. NMR showed a total of 32%$_{at}$ surface Si atoms.

As anticipated in the Introduction, both the typical hexagonal *P6mm* symmetry, and the unusual tetragonal *P4mm* symmetry were considered when computer models were prepared (see the Methods). In addition, when either the BJH or DFT theory was applied to analyze the N_2 adsorption isotherm (vide supra) a significantly different value for the pore diameter, d_p, was obtained. On these basis, four different in-silico models were built, whose geometrical parameters are summarized in Table 2.

Table 2. Geometrical parameters of the mesostructured silica simulated in this work. Lengths are in nanometer units.

Model[a)]	Symmetry	d_{100}[b)]	a_0[c)]	d_p[d)]	w[e)]	Box edges[f)] (x, y, z)	Number of atoms[g)]
MCM-41/BJH	P6mm	3.8	4.4	2.4	2.0	4.3x7.9x2.2	3472
MCM-41/DFT	P6mm			3.4	1.0		2352
t-MCM-41/BJH	P4mm	n.a.		2.4	2.0	6.4x6.4x2.2	4390
t-MCM-41/DFT	P4mm			3.4	1.0		3106

[a)] After the forward slash, the theory used to experimentally determine the pore diameter is indicated. An initial lowercase t is used to indicate transformation to tetragonal symmetry; [b)] Lattice spacing; not applicable to tetragonal symmetry; [c)] Interpore distance; [d)] Pore diameter; [e)] Wall thickness; [f)] Small difference (1-3 Angstrom) from the geometrically defined edges (see the Methods) originated from the use of the unit cell of β-cristobalite as the building block to construct the starting box filled with silica; [g)] Gas molecules are not included; they are inserted in the simulation box at a later stage.

When these four computer models were constructed (see the Methods), by hydrogenating all the surface O atoms, a quite different $\frac{Q^2+Q^3}{Q^2+Q^3+Q^4}$ ratio was obtained, as reported in Table 3.

Table 3. Relative amount of bulk (Q^4) and surface (Q^3+Q^2) Si atoms in the computer models of MCM-41.

Model[a)]	Symmetry	Number of Si atoms		Surface Si [%$_{at}$]	SSA[b)] [m^2 g^{-1}]
		Q^4	Q^3+Q^2		
MCM-41/BJH	P6mm	836	192	18.7	345
MCM-41/DFT	P6mm	424[c)]	188[c)]	30.7[c)]	689[c)]
t-MCM-41/BJH	P4mm	1170	180	13.3	274
t-MCM-41/DFT	P4mm	618	248	28.6	573

[a)] After the forward slash, the theory used to experimentally determine the pore diameter is indicated. An initial lowercase t is used to indicate transformation to tetragonal symmetry; [b)] Specific Surface Area; [c)] When this model was per-hydrogenated, Q^4 were 380, Q^3+Q^2 were 232, for a total of 37.9%$_{at}$ surface Si. SSA was 793 m^2 g^{-1}. In order to match the NMR results, a number of -Si-O-Si- bridges were created at random positions (see the Methods).

It is important to stress that all the models resulted in a number of surface Si atoms insufficient to match the NMR results (thus, the only option was to hydrogenate all surface O atoms), but the per-hydrogenated MCM-41/DFT (see Table 3 footnotes), with the correct space group symmetry (*P6mm*) and the pore size corresponding to the DFT analysis of the experimental N_2-physisorption isotherm. This was the only model having a number of surface Si atoms larger than the experimental ^{29}Si-NMR result, for which it was possible to match the latter by creating a number of -Si-O-Si- bridges at random positions (see the Methods). Finally, for the sake of future comparison, it is interesting to note the almost comparable final amount of surface Si in the MCM-41/DFT and t-MCM-41/DFT models, with the tetragonal one showing a slightly lower value. Thus, the largest apparent difference among these two was just the space group symmetry. Overall, the two models based on the BJH analysis of the experimental N_2-physisorption isotherm, resulted in a number of surface Si remarkably lower than the NMR result and the corresponding DFT-based models, suggesting that the BJH-predicted pore size was too. Again, the model with tetragonal symmetry showed the lowest value.

In Table 3, the specific surface area of the four computer models is also reported. The two BJH-based models have the smallest SSA, by virtue of the smaller pore size and the correspondingly wider bulk material in the simulation box. When the same pore size is taken with different symmetry: the more surface silanol groups, the larger the surface roughness, and the larger the SSA. The MCM-41/DFT model resulted to be the only one approaching the experimental BET SSA of 877 $m^2\ g^{-1}$. It is worth mentioning that, although BET is still of general use, its accuracy has been argued.[17] When SSA was experimentally determined through DFT analysis of the N_2-physisorption isotherm, 725 $m^2\ g^{-1}$ was obtained, which is in good agreement with our computer model. These differences among the four models, namely, pore size, symmetry, and the amount of silanol groups on the pore surface, affect the N_2 adsorption process, as shown by the N_2 density profiles in **Figure 3**.

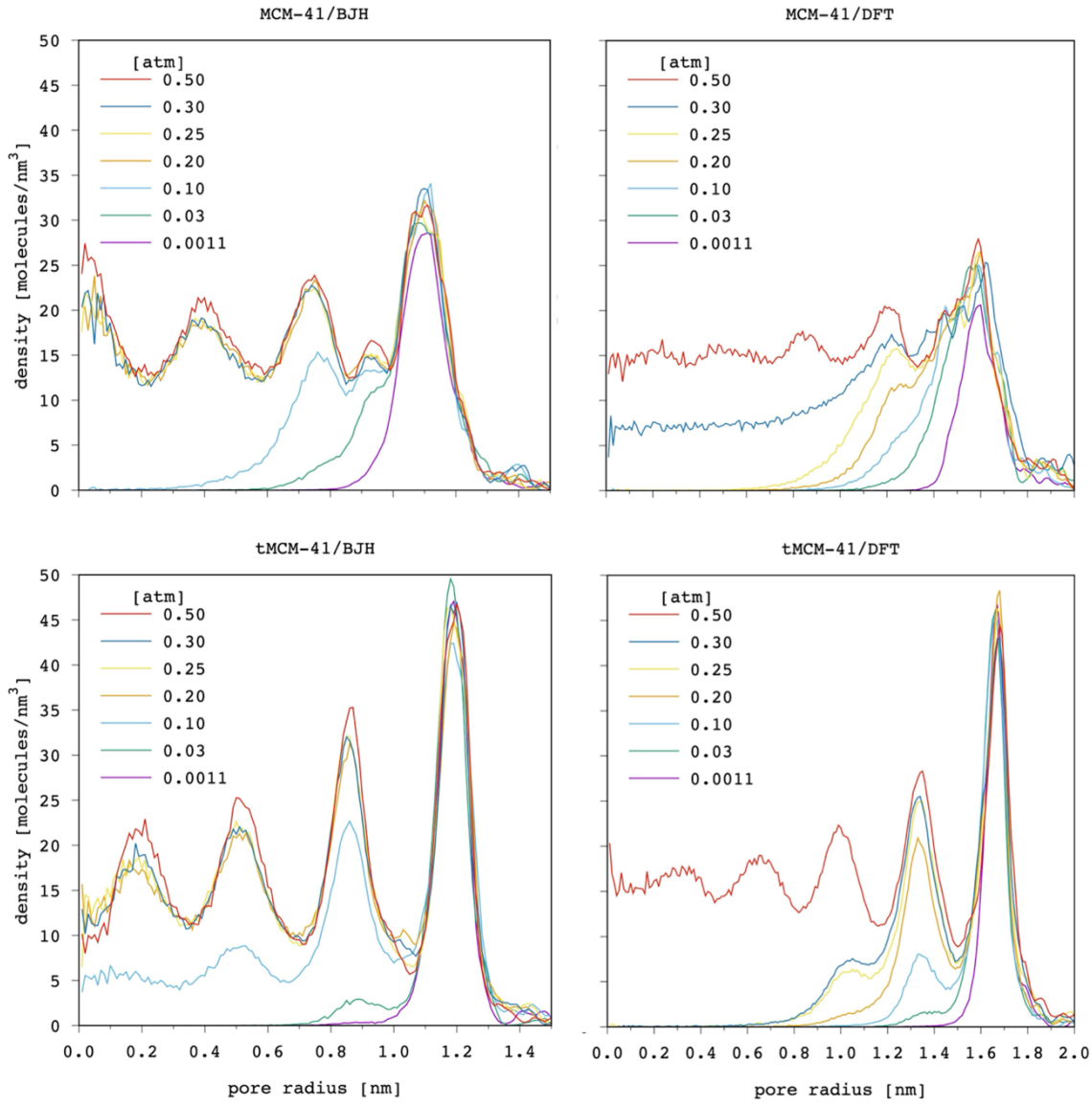

Figure 3. N_2 density profiles obtained from combined GCMC+MD simulations of the 4 investigated MCM-41 models at different pressure and 77 K. For the sake of clarity, the results from several selected pressure values are shown.

Progressive N_2 adsorption was observed with increasing pressure in all models. At low pressure values, a single layer was gradually formed on the pore surface. Then, with increasing the pressure, the density profiles broadened with further peaks progressively appearing at lower and lower values of the pore radius. Eventually, N_2 condensed inside the pores, as shown by non-zero density at the pore center, such that the multi-peak profile of the density curves is superimposed to an almost uniform background. Regardless of the model, the peaks were uniformly separated along the pore radius with a characteristic separation of about 0.34 nm. This value is in agreement with the Van der Waals diameter of the N_2 molecule (0.32 nm; see

the Methods), suggesting that the adsorbed phase was characterized by a layered structure, where each successive layer gradually formed after the previous one was almost completely saturated. Although this aspect of the N_2 adsorption process appeared to be pore size and symmetry independent, important differences are observed in Figure 3. The smaller pore radius of the two BJH-based models caused N_2 to condense at lower pressure, as it was already reported in the literature for this and other gases.[39–41] More interestingly, even when the pore size is the same, the change from *P6mm* to *P4mm* symmetry appeared to have a significant impact on the density profiles as a function of pressure. First, condensation occurs at a different pressure. Second, peaks are sharper in the two tetragonal models, suggesting a more ordered layered structure of the adsorbed phase. It is interesting to note, indeed, that in both hexagonal models, a minor peak or a shoulder is present on the left-hand side of the first adsorbed layer. This feature completely disappears in the two corresponding tetragonal models, which are characterized by a narrower and taller first adsorption peak instead. These changes will be discussed in more details from a microscopic point of view (vide infra).

These results are comprehensively reflected by significantly different simulated N_2 adsorption isotherms, which are shown in **Figure 4**.

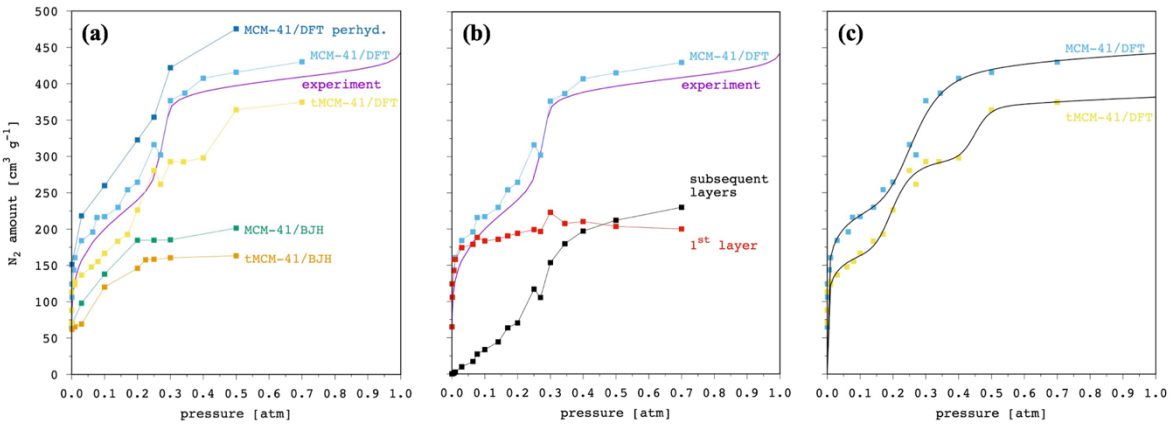

Figure 4. (a) The simulated N_2 adsorption isotherms obtained for different models of MCM-41 are shown (data points combined by lines) and compared to the experimental result. **(b)** The best reconstructed isotherm is shown together with the separated contributions from the 1st adsorbed layer and the other gas layers, respectively. **(c)** The simulated isotherm for MCM-41/DFT and tMCM-41/DFT are shown again (only data points), together with interpolation curves as guide to the eye.

The smaller pore diameter of both BJH-based models resulted in N_2 condensation to occur at significant lower pressure than observed in the experiment. Moreover, the very low relative

amount of surface silanol groups, reflected by the remarkably low SSA, resulted in a poor adsorption capacity of the two BJH-based models when compared to the real sample. These observations bolster the opinion that DFT, rather than BJH, ought to be applied to the analysis of experimental gas adsorption isotherms of materials with regular porous structure, such as MCM-41, as confirmed by different authors.[16,36] Indeed, it has been reported that the BJH method, based on the Kelvin equation, significantly underestimates the maximum of the PSD by about 1 nm (25%). This is because this model does not take the pore curvature into account, which has remarkable effects on the capillary condensation phenomena in the case of very small mesopores like in MCM-41. Nevertheless, BJH is widely used in the field, although evidence is being collected, this work included, that DFT allows to retrieve pore size distribution with higher accuracy. In fact, the comparison between PSD models, such as BJH, DFT-based models, BdB, and other methods based on XRD data or geometrical features (Gurvitch method),[42] has highlighted that DFT-based models are the most reliable in evaluating the pore diameter.[35]

Figure 4a also shows the results for the per-hydrogenated MCM-41/DFT model, i.e., before any -Si-O-Si- bridge was formed on the pore surface. This model had the largest amount of silanol groups (38%$_{at}$) and the correspondingly larger SSA (793 $m^2 g^{-1}$). Condensation occurred in the same pressure range as observed in the experiment, as shown by the inflection, because this feature is mostly determined by the pore size. However, the overall adsorption capacity of the model was clearly too high. These results show that the SSA obtained with the BET (877 $m^2 g^{-1}$) is too large. None of the models could reach such a large value. In fact, from our simulations, we can infer that adsorption capacity would have been even larger in such instance, deviating from the experimental data even more than our per-hydrogenated MCM-41/DFT model. These observations bolster the conclusion that BET method can lead to erroneous evaluation of the SSA and that other more sophisticated and accurate methods, like DFT, ought to be applied.[17]

The MCM-41/DFT model (after -Si-O-Si- bridge formation) included all the experimentally derived parameters, namely, the pore size, d_{100} lattice parameter, 2D hexagonal symmetry, pore-wall thickness, SSA, and the correct $\frac{Q^2+Q^3}{Q^2+Q^3+Q^4}$ ratio. Indeed, this model provided a simulated N_2 adsorption isotherm in very good agreement with the experimental one (Figure 4a,b). When the first adsorption peak of the density profile (Figure 3) was integrated to separate its contribution from the whole profile, together with the advantage of 3D visualization of the simulation trajectories, the different portions of the adsorption isotherm could be microscopically interpreted (Figure 4b). At low pressure, N_2 molecules adsorb on the pore surface through direct contacts with the silanol groups. The adsorbed amount rapidly increases until the available

surface is almost saturated. Then, the second layer of N_2 molecules starts to gradually form, through the interaction with the already adsorbed molecules of the first layer. The condensation process is cooperative,[43,44] as shown by the third and further layers easily forming on the second one before it is saturated, which is reflected by the marked inflection of the adsorption isotherm.

The tMCM-41/DFT model allows to inspect the effects of changing the pore symmetry from hexagonal to tetragonal, by keeping pore radius and wall thickness identical. The lower relative amount of silanol groups and the corresponding lower SSA explain the lower adsorption capacity with respect to the hexagonal model. More interestingly, the adsorbed layers appear to be more ordered, as discussed before (Figure 3), and the formation of the successive layers, up to the third one, occurs more gradually. The resulting isotherm (Figure 4c) is unusual for mesoporous materials. It is characterized by two successive inflections, resembling the IUPAC type VI adsorption isotherm, which is indicative of layer-by-layer adsorption and typical for highly uniform nonporous surfaces.[34] However, we found a report where a similar behavior was observed for water adsorption on some mesoporous materials from the TMPS family.[45] Unfortunately, the few reports on *P4mm* mesostructured silica we are aware of, do not show any N_2 or other gases adsorption isotherm.[27–33]

From the microscopic point of view, the largest difference between the MCM-41/DFT and tMCM-41/DFT models is the surface density of silanol groups, with that of the former (9.4 μmol m^{-2}) lower than the latter (10.4 μmol m^{-2}). **Figure 5** shows the distribution of the orientation assumed by the N_2 molecules in the first adsorbed layer (described through the θ and ϕ angles defined in **Figure 6**) at two selected pressure values.

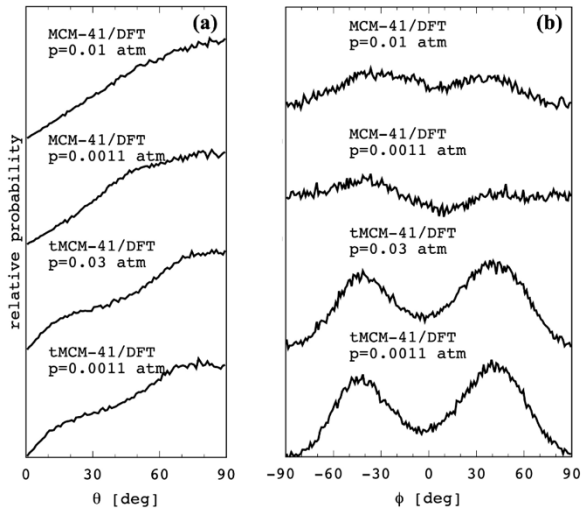

Figure 5. Distribution of N_2 molecules orientation inside the pores of the MCM-41/DFT and the tMCM-41/DFT models is shown for selected pressure values. Orientation was quantified

through the θ and ϕ angles defined in Figure 6. The angle θ is the one between the main inertia axis of the gas molecule and the pore axis; ϕ is the angle between the projection on the xy-plane of the main inertia axis of the gas molecule and the pore radius passing through the center of mass of the molecule.

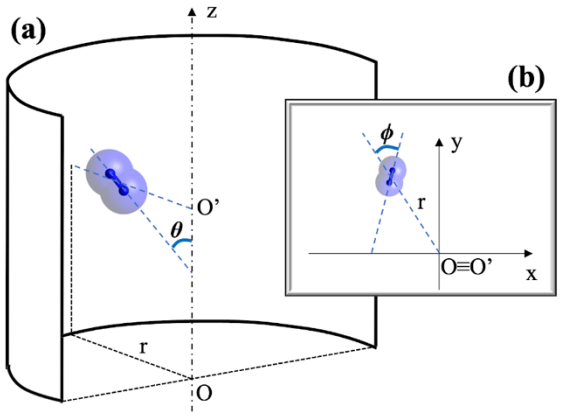

Figure 6. The angles use to describe gas molecule orientation (N_2 as example) with respect to the pore surface are shown. **(a)** θ is the plane angle between the main molecular inertia axis and the z-axis of the Cartesian coordinate system; **(b)** ϕ is the plane angle between the projection on the xy-plane of the main molecular inertia axis and the pore radius passing through the center of mass of the molecule.

The lowest inspected pressure was as low as 0.0011 atm, in order to have a nearly saturated first adsorbed layer with virtually no contributions from the second one. The highest silanol group density of the *P4mm* model is reflected by a more ordered layer of gas molecules. N_2 molecules are more tightly packed in the adsorbed layer, with correspondingly less degrees of freedom, as it is reflected by the slightly narrower distribution of the θ angle around 90° (i.e., gas molecules are found to be preferentially perpendicular to the pore axis) and, especially, by the well-defined bimodal distribution of the ϕ angle. The latter is almost symmetric with respect to 0°, with maxima located at about ±40°. Differently, the lower silanol group density of the *P6mm* model is reflected by a broader θ and a poorly defined, almost flat ϕ distribution. This is due to the "free space" between regions of the pore surface where silanol groups are clustered, leaving N_2 molecules with a superior orientational freedom, with respect to the tetragonal model. When the *P4mm* model was inspected at higher pressure (0.03 atm; Figure 5), such that the first adsorbed layer was fully saturated, both θ and ϕ distributions resulted to be quite comparable

to the corresponding ones at the lowest pressure, bolstering the high order of the N_2 molecules imposed by the high density of silanol groups on the pores' surface. Conversely, in the case of the *P6mm* model, we selected 0.01 atm, in order to investigate the growing shoulder on the left-hand side of the first peak in the density profiles (Figure 3), which is absent in the *P4mm* profile. After silanol groups are saturated, further N_2 molecules preferentially accommodate in the above mentioned "free space" between silanol group clusters. In fact, the shoulder in the density profile is located at a radius value between the first and the second N_2 layer. These molecules complete, in fact, the first adsorbed layer and, by filling the voids on the pore surface, they force the entire layer to assume a tighter and more ordered packing, which can be seen especially by the ϕ distribution in Figure 5, which tends to become comparable to those obtained for the *P4mm* model.

The enthalpy variation was estimated by analyzing the simulations performed at pressure values between 0.00011 and 0.03 atm, in order to focus on the gas-solid adsorption (i.e., only the first layer of N_2 molecules was formed). ΔH_{ads} resulted to be comparable for the two models within the precision of the method employed, with values of -10.9±0.7 and -9±2 kJ mol^{-1}, for MCM-41/DFT and tMCM-41/DFT, respectively. **Figure 7** shows the Gibbs free energy variation over the same pressure range.

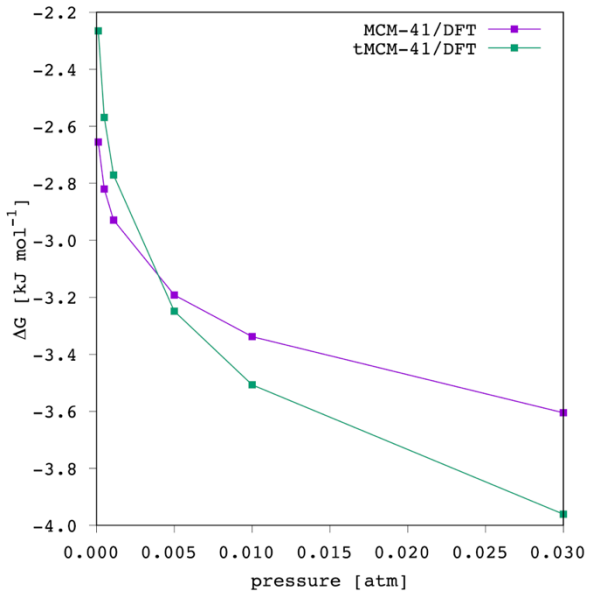

Figure 7. The ΔG_{ads} is shown as a function of pressure during the adsorption of the first N_2 layer for both the MCM-41/DFT and the tMCM-41/DFT models.

As widely reported,[35] N_2 adsorption on the solid surface of MCM-41 is an exothermic process, which makes it spontaneous at low temperature, while desorption is favored with increasing the

temperature. The variation of Gibbs free energy is negative but $|\Delta G_{ads}|<|\Delta H_{ads}|$, meaning that variation of entropy is negative and acts against spontaneity of the process. By using the average ΔH_{ads} value of -10 kJ mol^{-1}, average ΔS_{ads} can be estimated as -0.09 kJ mol^{-1} K^{-1}. As discussed before, when pressure is very low, N_2 molecules are more ordered in the *P4mm* than in the *P6mm* model. This is reflected by the latter being characterized by a more negative ΔG_{ads}. However, with increasing the pressure, entropy decreases for the *P6mm* model. Moreover, although the method for ΔH_{ads} determination was not quite precise, we can speculate that enthalpic contribution provided by the additional molecules that complete the first layer is lower, since the latter, as discussed, fill in the voids between silanol groups clusters and do not intimately interact with the solid surface. These differences in the mechanism of formation of the N_2 adsorption layer in the two materials are reflected by the inversion of the curves in Figure 7.

3. Conclusion

The present investigation addressed for the first time the effect of changing the symmetry of a mesostructured silica-based material from the typical hexagonal *P6mm* to the unusual tetragonal *P4mm*. Although methods to prepare and tailor the latter were already reported in the literature since 2009,[27–33] this is the first investigation about their performance as gas sorbents in comparison with the most common *P6mm* materials. The microscopic details of the N_2 adsorption process were correlated with each other to explain the macroscopic adsorption isotherm. The key feature making the greatest difference appeared to be the surface density of the silanol groups inside the mesopores. On the basis of the present investigation, the *P4mm* material exhibited a more ordered layer-by-layer adsorption process, which was reflected by the type VI instead of type IV N_2 adsorption isotherm. These results of theoretical simulations call for further experimental investigations and proofs, as well as studies on further gaseous species.

The present work also confirmed two important questions: (i) the BET method to determine the SSA is questionable for this class of mesoporous materials, while DFT methods allow more reliable results;[17] (ii) the BJH model resulted to be remarkably inaccurate and significantly underestimated the pore size, when compared to the DFT model.[16,35,36]

Overall, the presented MCM-41/DFT computer model was able to accurately reproduce the experimental adsorption isotherm. This result was possible only by including all the available information from complementary experimental techniques within the same computer model. In

conclusion, we want to stress this point, because a single technique would not have been sufficient.

4. Experimental Section/Methods

4.1 Chemicals

All chemicals were of analytical grade and used as received without further purification. Hexadecyltrimethylammonium bromide (CTAB, 98%), ethanol (EtOH, azeotropic 95.6%), ammonium hydroxide (NH_4OH, 28% NH_3 in H_2O), tetraethyl orthosilicate (TEOS, 98%), were purchased from Sigma-Aldrich. Distilled water was used for all the experiments.

4.2 MCM-41 Preparation

As previously reported in other works of some of the authors,[46,47] 1 g of the template agent (CTAB) in 200 mL of distilled water was kept at room temperature under continuous stirring for 180 minutes. EtOH (87 mL), and NH_4OH (21 mL) were added to the resulting micellar solution and stirred for additional 20 min. Then, stirring rate was increased and TEOS (3.8 mL) was suddenly added. After 1 hour stirring, the dispersion was transferred into an autoclave and treated at 373 K for 24 hours. The solids were separated by centrifugation, washed three times with a mixture of EtOH and H_2O, dried overnight at 353 K and then calcined at 823 K for 4 hours (heating rate, 5 K min^{-1}) to remove the organic template.

4.3 Experimental characterization

Low-angle (2θ = 0.9°–6.0°) X-ray diffraction (LA-XRD) patterns were recorded on a Seifert instrument with a θ-θ geometry and a Cu Kα anode. The lattice parameter (a_0) for the hexagonal porous structure was evaluated according to $a_0 = 2d_{100}/\sqrt{3}$, where d_{100} is the d-spacing of the hexagonal structure (vide infra, section 4.4). Textural analyses were carried out on a Micromeritics 2020 system by determining the nitrogen adsorption–desorption isotherms at 77 K. Prior to analyses, the samples were heated for 12 hours to 523 K under vacuum (heating rate, 1 K min^{-1}). The Brunauer–Emmett–Teller (BET) specific surface area (SSA) was calculated from the adsorption data in the p/p_0 range 0.05-0.17 (linearity, Rsq=0.99996 and C value 77.95). SSA was also estimated in accordance with the density functional theory (DFT) model. The total pore volume was calculated at the point p/p_0 = 0.99. Average pore diameter (d_p) was determined by applying either the Barrett−Joyner−Halenda (BJH) model to the isotherm desorption branch, or the DFT model (by assuming N_2 as the adsorptive gas, cylindrical pores,

and an oxide-based surface) to the isotherm adsorption branch. The wall thickness (w) was calculated as the difference between the lattice parameter (a_0) and the pore diameter (d_p).

TEM images were obtained by means of a JEOL JEM 2010 UHR microscope equipped with a Gatan Imaging Filter (GIF). Finely ground sample was dispersed in ethanol and sonicated, and the obtained suspension was then dropped on carbon-coated copper grids.

^{29}Si-MAS solid-state NMR spectra were acquired on the MCM-41 powder packed in a 2.5 mm diameter MAS rotor (internal volume 14 µL). Spectra were recorded at 300 K on a Bruker Avance III HD 600 (Bruker, Billerica, MA, USA) operating at a ^{1}H frequency of 600 MHz (^{29}Si: 119.23 MHz). Spectra were acquired at 10 kHz spinning rate, by using a 1.8 µs pulse (30°), 60 s delay time, 10 ms acquisition time, and a spectral width of 50 kHz for 1700 transients. Octakis(trimethylsiloxy)silsesquioxane (Q8M8) was used as an external reference to calibrate the chemical shift scale, by setting its high frequency ^{29}Si resonance at +12.6 ppm. Spectra processing and analysis, including deconvolution, were carried out with the software iNMR v.6.4.4 (MestreLab Research, Santiago de Compostela, Spain).

4.4 Simulation box preparation

The three-dimensional structure of MCM-41, with 2D hexagonal symmetry of identical cylindric mesopores, was obtained by following a procedure similar to what is presented in the literature for this and other mesostructured silica-based porous materials.[20,24] By starting from the experimentally (LA-XRD) determined lattice spacing (d_{100}), the unit cell parameter (a_0), i.e., the interpore distance, can be determined through simple geometrical considerations. However, knowledge of the space group symmetry is fundamental. In this work, we modelled either the typical hexagonal *P6mm* symmetry, and the unusual tetragonal *P4mm* symmetry (**Figure 8**).

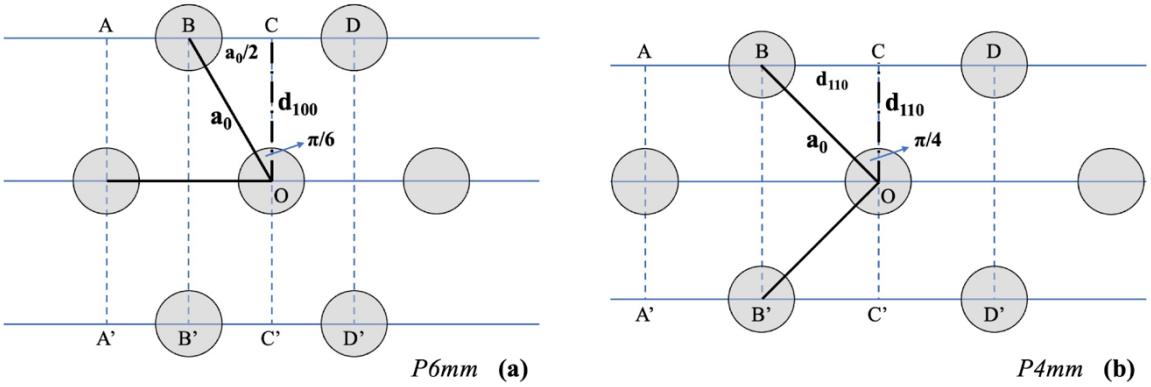

Figure 8. The 2D pore symmetry is shown as the xy-projection corresponding to **(a)** the hexagonal *P6mm* and **(b)** the tetragonal *P4mm* space group. Pores are shown as gray circles (pore axis is parallel to the z-axis). One series of selected planes crossing the pores is

represented as solid blue lines and the corresponding lattice spacing, d_{ijk}, is indicated with a long-dash-point black bold line. One series of perpendicular planes crossing the pores is shown with dashed blue lines. Selected intersection points on the xy-projection are labeled with uppercase letters. The interpore distance, a_0, is shown from the central reference pore to two of its nearest neighboring pores, as an example, and it was set to be identical in the two panels. The value of the plain angle formed by the indicated d_{ijk} and a_0 is shown.

MCM-41 has a *P6mm* symmetry (Figure 8a), so that $d_{100}=a_0\cos(\pi/6)=a_0(\sqrt{3}/2)$; $a_0=2d_{100}/\sqrt{3}$. It can be seen that $a_0=2r_p+w$, where r_p is the pore radius and w is the wall thickness. Every pore has 6 closest neighboring pores at a_0 distance. The xy-projection of the minimum orthogonal simulation box will be rectangular with $x=a_0$ and $y=2d_{100}$. Two alternative choices are possible: either the ACC'A' or the BDD'B' rectangle. These share identical area and a total of 2 pores, 4 half pores or, 1 pore and 4 quarters of a pore, respectively. We selected the former in this work. Periodic boundary conditions are applied in all the three dimensions of the system. When the number of closest neighboring pores is decreased from 6 to 4, the system changes from *P6mm* to *P4mm* symmetry (Figure 8b). By keeping a_0 constant, a shorter d_{ijk} results, where Miller indexes are not 100 anymore but 110, and $d_{110}=a_0\cos(\pi/4)=a_0(\sqrt{2}/2)$. The most important feature to note is that in the *P4mm* symmetry, the xy-projection of the minimum simulation box will be square with $x=y=2d_{110}$.

Starting from the unit cell of β-cristobalite,[48] available on the Encyclopedia of Crystallographic Prototypes on-line (http://aflowlib.org/prototype-encyclopedia/A2B_cF24_227_c_a.html), this was replicated along the three dimensions up to the desired value for the box edges. This starting material was chosen since its density (2.3 g/cm^3) is close to the reported density of the amorphous silica (2.2 g/cm^3).[49] The four half-pores were obtained by eliminating all the atoms found within a cylindrical volume with the desired radius (Table 2), the axis parallel to the z-axis of the Cartesian coordinate system, and located in the middle of each of the four faces perpendicular to the xy-plane. The resulting unsaturated Si atoms were eliminated, then, the resulting isolated O atoms were also eliminated, in order to preserve the surface chemistry. The remaining surface O atoms were bound to one single Si atom as part of a Q^3 or Q^2 site (where the index refers to the number of -O-Si-O- linkages to the material bulk). These were differently treated through an in-house computer code, to attain the SS-NMR experimental $\frac{Q^2+Q^3}{Q^2+Q^3+Q^4}$ ratio. Briefly, one surface Si was randomly selected, then, its nearest surface Si neighbors were identified. One Si was randomly selected

out of the latter. One surface O was selected for both the first and the second Si atoms and used to form a new -Si-O-Si- bridge. In practice, the two selected O atoms were removed, and one new O atom was placed between the two selected Si atoms. It is worth noting that, whenever a Q^2 site was transformed in this way, it turned into a Q^3; whenever a Q^3 was transformed, it became a bulk-like Q^4 site. After the desired number of new -Si-O-Si- bridges was formed, all the remaining surface O were hydrogenated, obtaining the surface -Si-OH groups.

Finally, the entire material was subjected to an amorphization stage, by applying a random maximum displacement of 0.5 Angstrom to each atom. Energy minimization was performed with 1000 steps of conjugate-gradients algorithm. Then, equilibration was carried out with classical Molecular Dynamics (MD) in the NVT ensemble, with 2.0 fs time-step, and by generating velocities according to the Boltzmann distribution at 1 K. Temperature was gradually increased up to 77 K during 20 ps of simulation, then, kept at 77 K for additional 100 ps. Temperature was controlled with the Nose-Hoover thermostat with a tdamp of 100. The time integration algorithm was the velocity Verlet as reported by Tuckerman et al.[50] Equations of motion were applied as formulated by Shinoda et al.[51] The O and Si atoms were subjected to positional constraint by applying a linear potential on x, y and z independently. Force constant was 1,000.0 kcal mol^{-1} $Å^{-1}$. The Shake algorithm[52] was applied to both O-H stretching and Si-O-H bending. No potential was applied to the torsion around Si-O bond. All the simulations were carried out with LAMMPS[53,54] (https://www.lammps.org).

4.5 Gas adsorption simulation

In order to insert N_2 gas molecules into the material pores and to equilibrate the gas/solid system at the given temperature and pressure, a combined Monte Carlo (MC) / MD approach was applied. A MC simulation scheme was applied, at first, in the Grand Canonical ensemble (GCMC) without any displacement or rotation move. Only gas molecules insertions and deletions were attempted inside the pores (1 of each kind on average at every step) for 2,500 steps. Then, 75,000 steps (150 ps) of equilibration MD followed in the NVT ensemble as described above. Gas molecules were treated as rigid bodies. This GCMC+MD scheme was iterated up to equilibrium, i.e., when the number of gas molecules in the simulation box fluctuated around a constant value for, at least, 100,000 GCMC consecutive steps. Temperature was 77 K. Pressure of the imaginary ideal gas reservoir during the GCMC, was in the range 1.1×10^{-4} – 0.7 atm. New velocities were generated at each run (both GCMC and MD) and the seed for the random number generator was often changed (both for velocities and GCMC moves) in order to bolster stochastic sampling of the phase space. Finally, the production MD

run was carried out in the NVT ensemble for 1 ns, whose trajectory was analyzed as described below. To determine the adsorption enthalpy (ΔH_{ads}; vide infra) an additional production run was performed by starting from the same equilibrated gas/solid system, with the combined GCMC+MD iterative scheme described above (100 repetitions), and saving the last frame of each NVT run for the analysis.

4.6 Force-field potentials and parameters

Harmonic potential was applied for both bond stretching and angle bending during the MD simulations to describe the -Si-O-H surface groups, whose parameters were reported by Bigot and Peuch.[55] The bulk material was subjected to positional restraints as described above. Gas molecules were treated as rigid bodies. Bonds and angles potentials, as well as bulk positional restrains, were switched off during GCMC. Non-bonded interactions were described by a sum of Lennard–Jones and Coulomb potentials, whose parameters were reported by Furukawa et al.[23] It is worth mentioning that for the bulk SiO_2, only the O atoms have non-zero LJ parameters, since the role of Si atoms on gas adsorption is negligible.[23,56] Non-bonded interactions were calculated by using a double cutoff, with values of 12.0 Å and 14.0 Å. Long-range Van der Waals tail correction to the total energy was applied as formulated by Sun,[57] and as suggested by Shah et al.[58,59] The Particle-Particle Particle-Mesh method[60] was applied to calculate long range electrostatics. A screening parameter of $\kappa = 3.2/\text{cutoff}$ and an upper bound of the reciprocal space summation at $K_{max}=\text{int}(\kappa L_{box})+1$ were used, as reported by Shah et al.[58,59] The N_2 molecules were described with the TraPPE force-field reported by Potoff and Siepmann.[61] It is worth noting that N_2 quadrupole moment was modelled by placing one charged dummy atom in the center of mass with no LJ parameters, in addition to the two N atoms.

4.7 Trajectory analysis

Gas molecule density profile was reconstructed as a function of the pore radius for each pressure, through an in-house computer code. Gas molecules were assigned to each half-pore by their Euclidean distance perpendicular to the pore axis, then, they were counted and assigned to coaxial cylindrical layers with different radius. Gas molecule density as a function of the pore radius was obtained by dividing the number of gas molecules in each layer by 4 times the volume of that layer. The integral of the density profile was numerically calculated, the number of molecules was converted into moles, and the value multiplied by the molar volume of the ideal gas (cm^3/mol) at STP conditions and by the material SSA ($Å^2/g$), to obtain the amount of

adsorbed gas in cm^3/g to be compared with the experimental adsorption isotherm data points. The surface area was evaluated for each model as the solvent accessible surface area by using the "get area" tool of PyMOL v2.5 (https://pymol.org/2/), with the largest accuracy (parameter dot_density set to 4) and by using a probe radius of 1.6 Å (calculated from the N_2 Van der Waals volume obtained by Chemicalize (https://chemicalize.com/ developed by ChemAxon, http://www.chemaxon.com). Above a certain threshold pressure, gas condensation was observed inside the pores (gas density at the pore center > 0), for which density profiles required bulk density (ρ_b) correction to recover the adsorbed amount to be compared with the experiments.[62–65] A sigmoid profile, $\rho_b = \frac{m(r_p-2p)^s}{(r_p-2p)^s+p^s}$; $m \geq 0$; $p \geq 0$; $s=2,4,6,\ldots$, where m is the maximum at $r_p \rightarrow 0$, p is the position of the falling point of inflection, and s modulates the slope at the inflection point, was chosen to subtract bulk density from the total integral. Orientation of the gas molecules in the adsorbed layers were evaluated with an in-house computer code, according to the angle definitions shown in Figure 6.

In particular, the distribution of the θ and ϕ angles were reconstructed, where θ is the plane angle between the main inertia axis of the gas molecule and the z-axis of the Cartesian coordinate system; ϕ is the plane angle between the projection on the xy-plane of the main inertia axis of the gas molecule and of the pore radius passing through the center of mass of the molecule.

The difference of the Gibbs free energy, Enthalpy and Entropy of the gas molecules in the adsorbed phase with respect to the gas reservoir at the same temperature and pressure were estimated as follows. Simulated adsorption isotherm data points were fitted with the combined Langmuir-Freundlich model:[66–69]

$$q(p) = \frac{abp^{1/n}}{1+bp^{1/n}} \quad (1)$$

where, q is the amount of gas adsorbed inside the pores, p is the pressure of the gas reservoir in equilibrium with the solid-gas system, and a, b and n are fitting parameters. This model is more flexible than either the Langmuir model, which assumes the homogeneous adsorption of a single gas layer where molecules adsorb on specific non-interacting sites, and the Freundlich one, which assumes heterogenous multi-layer adsorption.

The Gibbs free energy of adsorption was calculated according to the following equation, by using the curve-fitting results:[66]

$$\Delta G_{ads}(p_i) = -\frac{RT}{q(p_i)} \int_0^{p_i} \frac{q(p)}{p} dp \quad (2)$$

where, p_i is the i-th value of the pressure considered for the analysis. Integrals were calculated with the Desmos graphing calculator (https://www.desmos.com/).

The enthalpy of adsorption can be estimated from the fluctuations of the number of gas molecules during the GCMC simulation and of their configurational energy:[70]

$$\Delta H_{ads} = \frac{f(U_{ads},n_{ads})}{f(n_{ads},n_{ads})} - \langle U_g \rangle - RT \quad (3)$$

where, fluctuations are defined as $f(X,Y)=\langle XY \rangle - \langle X \rangle \langle Y \rangle$, U_{ads} is the total energy of the gas molecules inside the pores, n_{ads} is the number of gas molecules inside the pores, U_g is the potential energy of the gas molecule (in the gas phase) that is equal to zero for rigid bodies in ideal conditions.

Finally, adsorption entropy was calculated as:

$$\Delta S_{ads} = \frac{\Delta H_{ads} - \Delta G_{ads}}{T} \quad (4)$$

Acknowledgments

University of Cagliari and Fondazione di Sardegna are acknowledged for the financial support – project: "Surface-tailored materials for sustainable environmental applications" CUP F72F20000240007(2019). The Italian Ministry of University and Research (MUR) is greatly acknowledged for the PhD fellowship assigned to P.C.. Fluorsid S.p.A. is acknowledged for the post-doc fellowship of C.C.. Part of the computational work was performed using the resources of the computational chemistry laboratory (Chemistry Degree Course) of the University of Cagliari, realized with funding from the Sardinia Regional Government (P.O.R FESR 2007–2013, obiettivo competitività regionale e occupazione, asse I, società dell'informazione—linea di attività 1.2.2.c). Dr. Sandrina Lampis, Dr. Andrea Ardu, and the CeSAR (Centro Servizi d'Ateneo per la Ricerca) of the University of Cagliari are acknowledged for the NMR experiments and the TEM measurements.

Conflict of interest

The authors declare no conflict of interest.

Received: ((will be filled in by the editorial staff))
Revised: ((will be filled in by the editorial staff))
Published online: ((will be filled in by the editorial staff))

References

[1] Z. A. ALOthman, *Materials* **2012**, *5*, 2874.
[2] C. T. Kresge, M. E. Leonowicz, W. J. Roth, J. C. Vartuli, J. S. Beck, *Nature* **1992**, *359*, 710.
[3] J. A. S. Costa, R. A. de Jesus, D. O. Santos, J. B. Neris, R. T. Figueiredo, C. M. Paranhos, *Journal of Environmental Chemical Engineering* **2021**, *9*, 105259.
[4] M. A. Vacca, C. Cara, V. Mameli, M. Sanna Angotzi, M. A. Scorciapino, M. G. Cutrufello, A. Musinu, V. Tyrpekl, L. Pala, C. Cannas, *ACS Sustainable Chem. Eng.* **2020**, *8*, 14286.
[5] B. G. Trewyn, I. I. Slowing, S. Giri, H.-T. Chen, V. S.-Y. Lin, *Acc. Chem. Res.* **2007**, *40*, 846.
[6] C. Cara, V. Mameli, E. Rombi, N. Pinna, M. Sanna Angotzi, D. Nižňanský, A. Musinu, C. Cannas, *Microporous and Mesoporous Materials* **2020**, *298*, 110062.
[7] M. S. Angotzi, V. Mameli, C. Cara, K. B. L. Borchert, C. Steinbach, R. Boldt, D. Schwarz, C. Cannas, *Nanoscale Adv.* **2021**, *3*, 6100.
[8] E. Rombi, M. G. Cutrufello, C. Cannas, M. Casu, D. Gazzoli, M. Occhiuzzi, R. Monaci, I. Ferino, *Phys. Chem. Chem. Phys.* **2009**, *11*, 593.
[9] S. Varghese, M. G. Cutrufello, E. Rombi, C. Cannas, R. Monaci, I. Ferino, *Applied Catalysis A: General* **2012**, *443–444*, 161.
[10] C. Cara, F. Secci, S. Lai, V. Mameli, K. Skrodczky, P. A. Russo, F. Ferrara, E. Rombi, N. Pinna, M. Mureddu, C. Cannas, *Journal of CO2 Utilization* **2022**, *62*, 102066.
[11] J. S. Beck, J. C. Vartuli, W. J. Roth, M. E. Leonowicz, C. T. Kresge, K. D. Schmitt, C. T. W. Chu, D. H. Olson, E. W. Sheppard, S. B. McCullen, J. B. Higgins, J. L. Schlenker, *J. Am. Chem. Soc.* **1992**, *114*, 10834.
[12] J. C. Vartuli, K. D. Schmitt, C. T. Kresge, W. J. Roth, M. E. Leonowicz, S. B. McCullen, S. D. Hellring, J. S. Beck, J. L. Schlenker, *Chem. Mater.* **1994**, *6*, 2317.
[13] V. Alfredsson, M. Keung, A. Monnier, G. D. Stucky, K. K. Unger, F. Schüth, *J. Chem. Soc., Chem. Commun.* **1994**, 921.
[14] S. Brunauer, P. H. Emmett, E. Teller, *J. Am. Chem. Soc.* **1938**, *60*, 309.
[15] E. P. Barrett, L. G. Joyner, P. P. Halenda, *J. Am. Chem. Soc.* **1951**, *73*, 373.
[16] J. Landers, G. Yu. Gor, A. V. Neimark, *Colloids and Surfaces A: Physicochemical and Engineering Aspects* **2013**, *437*, 3.
[17] J. Condon, *Surface Area and Porosity Determinations by Physisorption. Measurements, Classical Theories and Quantum Theory.*, Elsevier, Amsterdam, **2019**.
[18] S.-C. Chang, S.-Y. Chien, C.-L. Chen, C.-K. Chen, *Applied Surface Science* **2015**, *331*, 225.
[19] Y. Jing, L. Wei, Y. Wang, Y. Yu, *Chemical Engineering Journal* **2013**, *220*, 264.
[20] L. N. Ho, J. Perez Pellitero, F. Porcheron, R. J.-M. Pellenq, *Langmuir* **2011**, *27*, 8187.
[21] F. R. Hung, S. Bhattacharya, B. Coasne, M. Thommes, K. E. Gubbins, *Adsorption* **2007**, *13*, 425.
[22] A. J. Palace Carvalho, T. Ferreira, A. J. Estêvão Candeias, J. P. Prates Ramalho, *Journal of Molecular Structure: THEOCHEM* **2005**, *729*, 65.
[23] S. Furukawa, T. Nishiumi, N. Aoyama, T. Nitta, M. Nakano, *Journal of Chemical Engineering of Japan* **2005**, *38*, 999.
[24] A. A. Sizova, V. V. Sizov, E. N. Brodskaya, *Colloids and Surfaces A: Physicochemical and Engineering Aspects* **2015**, *474*, 76.
[25] A. A. Sizova, V. V. Sizov, E. N. Brodskaya, *Colloids and Surfaces A: Physicochemical and Engineering Aspects* **2017**, *524*, 87.
[26] B. Coasne, A. Galarneau, F. Di Renzo, R. J. M. Pellenq, *Langmuir* **2006**, *22*, 11097.
[27] C. Jin, L. Han, S. Che, *Angewandte Chemie International Edition* **2009**, *48*, 9268.

[28] B. Liu, Y. Cao, Z. Huang, Y. Duan, S. Che, *Advanced Materials* **2015**, *27*, 479.
[29] L. Han, C. Jin, B. Liu, S. Che, *Chem. Mater.* **2012**, *24*, 504.
[30] B. Liu, Y. Yao, S. Che, *Angewandte Chemie International Edition* **2013**, *52*, 14186.
[31] B. Liu, L. Han, S. Che, *Interface Focus* **2012**, *2*, 608.
[32] Y. Yao, D. Wang, L. Han, S. Che, *Chemistry – A European Journal* **2013**, *19*, 15489.
[33] A. Azhati, H. Zhu, T. Ouyang, T. He, Y. Zeng, P. Wu, J. Jiang, H. Peng, S. Che, *Small* **2022**, *18*, 2107123.
[34] M. Thommes, K. Kaneko, A. V. Neimark, J. P. Olivier, F. Rodriguez-Reinoso, J. Rouquerol, K. S. W. Sing, *Pure and Applied Chemistry* **2015**, *87*, 1051.
[35] S. Lowell, J. E. Shields, M. A. Thomas, M. Thommes, *Characterization of Porous Solids and Powders: Surface Area, Pore Size and Density*, Springer, **2004**.
[36] F. Di Renzo, A. Galarneau, P. Trens, N. Tanchoux, F. Fajula, in *Studies in Surface Science and Catalysis* (Eds.: R. Aiello, G. Giordano, F. Testa), Elsevier, **2002**, pp. 1057–1066.
[37] E. Lippmaa, M. Maegi, A. Samoson, G. Engelhardt, A. R. Grimmer, *J. Am. Chem. Soc.* **1980**, *102*, 4889.
[38] M. Luhmer, J. B. d'Espinose, H. Hommel, A. P. Legrand, *Magn Reson Imaging* **1996**, *14*, 911.
[39] P. L. Llewellyn, Y. Grillet, F. Schüth, H. Reichert, K. K. Unger, *Microporous Materials* **1994**, *3*, 345.
[40] P. I. Ravikovitch, S. C. O. Domhnaill, A. V. Neimark, F. Schueth, K. K. Unger, *Langmuir* **1995**, *11*, 4765.
[41] T. Horikawa, D. D. Do, D. Nicholson, *Advances in Colloid and Interface Science* **2011**, *169*, 40.
[42] A. Galarneau, D. Desplantier, R. Dutartre, F. Di Renzo, *Microporous and Mesoporous Materials* **1999**, *27*, 297.
[43] S. Shimizu, N. Matubayasi, *Langmuir* **2021**, *37*, 10279.
[44] P. J. M. Carrott, R. A. Roberts, K. S. W. Sing, *Carbon* **1987**, *25*, 59.
[45] F. Miksik, T. Miyazaki, *Adsorption* **2019**, *25*, 1137.
[46] C. Cara, E. Rombi, A. Musinu, V. Mameli, A. Ardu, M. S. Angotzi, L. Atzori, D. Niznansky, H. L. Xin, C. Cannas, *J. Mater. Chem. A* **2017**, *5*, 21688.
[47] C. Cara, E. Rombi, V. Mameli, A. Ardu, M. Sanna Angotzi, D. Niznansky, A. Musinu, C. Cannas, *J. Phys. Chem. C* **2018**, *122*, 12231.
[48] *Zeitschrift für Kristallographie - Crystalline Materials* **1973**, *138*, 274.
[49] D. R. Lide, *CRC Handbook of Chemistry and Physics*, Taylor And Francis, Boca Raton (FL) - U.S.A., **2007**.
[50] M. E. Tuckerman, J. Alejandre, R. López-Rendón, A. L. Jochim, G. J. Martyna, *J. Phys. A: Math. Gen.* **2006**, *39*, 5629.
[51] W. Shinoda, M. Shiga, M. Mikami, *Phys. Rev. B* **2004**, *69*, 134103.
[52] J.-P. Ryckaert, G. Ciccotti, H. J. C. Berendsen, *Journal of Computational Physics* **1977**, *23*, 327.
[53] A. P. Thompson, H. M. Aktulga, R. Berger, D. S. Bolintineanu, W. M. Brown, P. S. Crozier, P. J. in 't Veld, A. Kohlmeyer, S. G. Moore, T. D. Nguyen, R. Shan, M. J. Stevens, J. Tranchida, C. Trott, S. J. Plimpton, *Computer Physics Communications* **2022**, *271*, 108171.
[54] S. Plimpton, *Journal of Computational Physics* **1995**, *117*, 1.
[55] B. Bigot, V.-H. Peuch, *J. Phys. Chem.* **1995**, *99*, 8206.
[56] J.-H. Yun, T. Düren, F. J. Keil, N. A. Seaton, *Langmuir* **2002**, *18*, 2693.
[57] H. Sun, *J. Phys. Chem. B* **1998**, *102*, 7338.
[58] M. S. Shah, M. Tsapatsis, J. I. Siepmann, *Langmuir* **2015**, *31*, 12268.
[59] M. S. Shah, M. Tsapatsis, J. I. Siepmann, *J. Phys. Chem. B* **2015**, *119*, 7041.

[60] R. Hockney, J. Eastwood, *Computer Simulation Using Particles*, CRC Press, **1988**.
[61] J. J. Potoff, J. I. Siepmann, *AIChE Journal* **2001**, *47*, 1676.
[62] Y. Tian, C. Yan, Z. Jin, *Sci Rep* **2017**, *7*, 12040.
[63] Y. Pang, X. Hu, S. Wang, S. Chen, M. Y. Soliman, H. Deng, *Chemical Engineering Journal* **2020**, *396*, 125212.
[64] L. Luo, L. Zuo, Y. Wei, *Adsorption Science & Technology* **2015**, *33*, 939.
[65] O. Talu, A. L. Myers, *AIChE Journal* **2001**, *47*, 1160.
[66] M. Hao, Z. Qiao, H. Zhang, Y. Wang, Y. Li, *Energy Fuels* **2021**, *35*, 4246.
[67] Y. Zheng, Q. Li, C. Yuan, Q. Tao, Y. Zhao, G. Zhang, J. Liu, G. Qi, *Fuel* **2018**, *230*, 172.
[68] Z. W. Zhu, Q. R. Zheng, *Applied Thermal Engineering* **2016**, *108*, 605.
[69] X. Xu, X. Zhao, L. Sun, X. Liu, *Journal of Natural Gas Chemistry* **2008**, *17*, 391.
[70] J. Zhao, S. Deng, L. Zhao, X. Yuan, Z. Du, S. Li, L. Chen, K. Wu, *Sustainable Energy Fuels* **2020**, *4*, 5970.

Table of Contents

The 3D model of MCM-41 is built by exploiting experimental data from real samples. Two different pores symmetries are considered: the canonical *P6mm*, or the rare *P4mm*. Grand-canonical Monte Carlo and molecular dynamics simulations are used to probe the microscopic-level differences. The surface-adsorbed gas molecules are differently ordered and a different type of N_2 adsorption isotherm is correspondingly found.

P. Carta, C. Cara, C. Cannas, M. A. Scorciapino*

Experiments-Guided Modeling of MCM-41: Impact of Pore Symmetry on Gas Adsorption